

Convolution Backprojection Formulas for 3-D Vector Tomography with Application to MRI

Jerry L. Prince, *Member, IEEE*

Abstract— Vector tomography is the reconstruction of vector fields from measurements of their projections. In previous work, it has been shown that reconstruction of a general three-dimensional (3-D) vector field is possible from the so-called inner product measurements. It has also been shown how reconstruction of either the irrotational or solenoidal component of a vector field can be accomplished with fewer measurements than that required for the full field. The present paper makes three contributions. First, in analogy to the two-dimensional (2-D) approach of Norton, several 3-D projection theorems are developed. These lead directly to new vector field reconstruction formulas that are convolution backprojection formulas. It is shown how the local reconstruction property of these 3-D reconstruction formulas permits reconstruction of point flow or of regional flow from a limited data set. Second, simulations demonstrating 3-D reconstructions, both local and nonlocal, are presented. Using the formulas derived herein and those derived in previous work, these results demonstrate reconstruction of the irrotational and solenoidal components, their potential functions, and the field itself from simulated inner product measurement data. Finally, it is shown how 3-D inner product measurements can be acquired using a magnetic resonance scanner.

I. INTRODUCTION

VECTOR tomography is the reconstruction of vector fields—e.g., the velocity of fluid flow or the displacement of a deformed object—from projections of components of the field. In this paper, we consider the following general projection measurement:

$$g^p(l, \omega) = \int_{\mathbb{R}^3} \mathbf{p}(l, \omega) \cdot \mathbf{q}(\mathbf{x}) \delta(l - \omega \cdot \mathbf{x}) d\mathbf{x} \quad (1)$$

which we call the *inner product measurement* or *probe transform* of vector field \mathbf{q} . The effect of probe $\mathbf{p}(l, \omega)$ is to convert the vector field $\mathbf{q}(\mathbf{x})$ into a scalar by taking a point-by-point inner product. The resultant scalar field is then integrated over planes as in the 3-D Radon transform. This transformation generalizes a type of measurement equation that has been studied in two dimensions and almost exclusively in the context of acoustic flow imaging using time-of-flight measurements—e.g., ultrasonic imaging in medicine [1], flow imaging in nondestructive evaluation [2], [3], and ocean acoustic tomography [4], [5]. In this application, the acoustic time-of-flight along a line is measured, reflecting a change

about its nominal value due to the component of fluid velocity along the line. It is a two-dimensional (2-D) problem (because it integrates on lines rather than planes) and is limited to a probe direction coinciding with the line of integration. Norton showed in [6] that only the divergence-free component of the field can be reconstructed from these measurements. More recently, Braun and Hauck [7] showed that use of an orthogonal probe allows one, in principle, to reconstruct the irrotational component as well. However, it is not known how to make acoustic probe transform measurements using orthogonal probes. Recently, Rouseff and Winters [8] formulated an acoustic flow measurement approach using physically realizable acoustic diffraction measurements. Their approach uses a different measurement model than (1) and is strictly 2-D.

More recently, Norton conceived of an optical analog of the time-of-flight acoustic imaging problem in which “the quantity measured is the change in optical path length of a collimated laser beam directed through the region of flow” [9]. In this technique, optical phase shifts arising from flow can be measured interferometrically leading to an analogous measurement as the acoustical time-of-flight measurements. Norton also described a new vector tomographic approach to flow measurement based on Doppler measurements, which might be either acoustical or optical. Juhlin independently proposed a Doppler approach and conducted simulations for its use in the reconstruction of blood flow in vessels [10]. Prince suggested that inner product measurements of three-dimensional (3-D) velocity fields can be made using magnetic resonance imaging techniques [11], a topic that is addressed further in the present paper. The concept that vector fields can be reconstructed from direction-dependent integral measurements has also been discovered in fields other than flow measurement. For example, Zahn proposed to reconstruct the electric field in a Kerr material by measuring the polarization of light passing through the sample from many directions [12]. In the monograph [13], Sharafutdinov proposed the use of optical polarization measurements to reconstruct material stress using the Brewster effect. The mathematical framework of the probe transform applies to special cases within these applications, although the general framework can be very much more complicated (cf., [13]). Because the number of applications is growing, there is a clear need to examine the general theoretical properties related to reconstructing vector fields from the probe transform.

The theory and practice of vector tomography has been studied in the past by several investigators. Johnson *et al.* [1] considered 3-D fluid velocity reconstruction from acous-

Manuscript received September 11, 1994; revised December 29, 1995. This work was supported by the National Institutes of Health under Grant R01-HL45090 and the National Science Foundation under Grant MIP93-50336. The associate editor coordinating the review of this manuscript and approving it for publication was Prof. Ken D. Sauer.

The author is with the Department of Electrical and Computer Engineering, Image Analysis and Communications Laboratory, The Johns Hopkins University, Baltimore, MD 21218 USA (e-mail: prince@jhu.edu).

Publisher Item Identifier S 1057-7149(96)06028-9.

tic transmission measurements. They developed a numerical approach and identified a lack of uniqueness in their solution. Norton [6] considered the 2-D problem, developed a 2-D projection theorem, and showed through Helmholtz's decomposition of vector fields that the irrotational component is invisible to standard line integral measurements. This accounted for the lack of uniqueness in Johnson *et al.*'s solution. Norton proposed boundary measurements to reconstruct the irrotational component separately under the assumption that there are no sinks or sources within the domain. Braun and Hauck [7] considered the 2-D problem again, independently developed the use of Helmholtz's decomposition, but proposed the use of another probe direction to recover the irrotational component. Their approach does not require the absence of sinks and sources, but the required measurements cannot be made using acoustical time-of-flight [9]. Prince [14] extended the results of Braun and Hauck to 3-D vector fields and to arbitrary probe directions. It was shown in [14] that the irrotational and solenoidal components of an arbitrary 3-D vector field can be reconstructed from the measurements obtained using one and two probes, respectively. Finally, Desbat and Wernsdorfer have developed an efficient direct algebraic reconstruction algorithm for 2-D vector tomography using an interlaced sampling scheme [15].

In this paper, we first develop a set of projection theorems for 3-D vector tomography. This theory confirms the main results in [14] using the frequency domain. The main theorem, which relates the 1-D Fourier transform of the probe transform to the 3-D Fourier transform of a component of the vector field, is then used to develop several new reconstruction formulas. These formulas are of the convolution backprojection variety, while those in [14] are not. While the formulas given here can be derived directly from those in [14], the Fourier approach given here is more straightforward and intuitively appealing. Furthermore, this approach starts from "first principles," rather than from an existing inverse 3-D Radon transform formula. Next, we present an extensive set of simulations to demonstrate the behavior of the new reconstruction formulas and also those of [14], in which no simulations were provided. Finally, we describe how the 3-D probe transform can be measured using a magnetic resonance scanner.

II. BACKGROUND

A. Radon Transform

The 3-D Radon transform of a scalar function $f(\mathbf{x})$, where $\mathbf{x} = (x, y, z) \in \mathbb{R}^3$, is defined as [16]

$$\check{f}(l, \boldsymbol{\omega}) = \mathcal{R}f = \int_{\mathbb{R}^3} f(\mathbf{x}) \delta(l - \boldsymbol{\omega} \cdot \mathbf{x}) d\mathbf{x} \quad (2)$$

where l is a real scalar parameter, $\boldsymbol{\omega}$ is a unit vector in \mathbb{R}^3 , and $\delta(\cdot)$ is the one-dimensional (1-D) Dirac delta function. The 3-D Radon transform of a 3-D vector field $\mathbf{q} = \mathbf{q}(\mathbf{x}) = [u(\mathbf{x}), v(\mathbf{x}), w(\mathbf{x})]$ is

$$\check{\mathbf{q}}(l, \boldsymbol{\omega}) = [\check{u}(l, \boldsymbol{\omega}), \check{v}(l, \boldsymbol{\omega}), \check{w}(l, \boldsymbol{\omega})]. \quad (3)$$

It is assumed here and throughout this paper that both f and the elements of \mathbf{q} belong to either \mathcal{L} , the class of

rapidly decreasing C^∞ functions, or \mathcal{D} , the class of C^∞ functions with compact support. This implies that all fields have homogeneous boundary conditions—i.e., they go to zero on the boundary. Unless otherwise indicated, vectors are designated using bold symbols and are assumed to be column vectors.

From (1) and (2), it follows that

$$g^{\mathbf{p}}(l, \boldsymbol{\omega}) = \mathbf{p}(l, \boldsymbol{\omega}) \cdot \check{\mathbf{q}}(l, \boldsymbol{\omega}). \quad (4)$$

This implies that for three probes \mathbf{p}_1 , \mathbf{p}_2 , and \mathbf{p}_3 , which are linearly independent at each $(l, \boldsymbol{\omega})$, we can recover the 3-D Radon transform of \mathbf{q} as follows:

$$\check{\mathbf{q}} = \begin{bmatrix} \mathbf{p}_1^T \\ \mathbf{p}_2^T \\ \mathbf{p}_3^T \end{bmatrix}^{-1} \begin{bmatrix} g^{\mathbf{p}_1} \\ g^{\mathbf{p}_2} \\ g^{\mathbf{p}_3} \end{bmatrix}. \quad (5)$$

In this equation and many of those that follow, explicit functional dependence on l and $\boldsymbol{\omega}$ is omitted for convenience. The vector field can be recovered using the inverse Radon transform [16], which can be symbolically written $\mathbf{q} = \mathcal{R}^{-1}\check{\mathbf{q}}$. Here, the inverse transform is applied separately to each element of the vector $\check{\mathbf{q}}$ to produce the vector \mathbf{q} . For our purposes, it is useful to write the inverse 3-D Radon transform of \check{f} as

$$f = \mathcal{R}^* \mathcal{K}' \check{f}_l, \quad (6)$$

where

$$\begin{aligned} (\mathcal{R}^* g)(\mathbf{x}) &= \int_{|\boldsymbol{\omega}|=1} g(\boldsymbol{\omega} \cdot \mathbf{x}, \boldsymbol{\omega}) d\boldsymbol{\omega} \\ \mathcal{K}' &= \frac{-1}{8\pi^2} \frac{\partial}{\partial l} \check{f}_l \\ &= \frac{\partial \check{f}}{\partial l}. \end{aligned}$$

B. Field Components

According to Helmholtz's theorem, a vector field $\mathbf{q}(\mathbf{x})$ with homogeneous boundary conditions can be uniquely written [17] as

$$\mathbf{q} = \mathbf{q}_I + \mathbf{q}_S \quad (7a)$$

$$\mathbf{q}_I = \nabla \psi \quad (7b)$$

$$\mathbf{q}_S = \nabla \times \mathbf{a} \quad (7c)$$

where $\nabla \cdot \mathbf{a} = 0$. The scalar function ψ is called the *scalar potential* and the vector function \mathbf{a} is called the *vector potential*. The *irrotational* component \mathbf{q}_I satisfies $\nabla \times \mathbf{q}_I = 0$, while the *solenoidal* component \mathbf{q}_S satisfies $\nabla \cdot \mathbf{q}_S = 0$.

It is convenient to give separate symbols to fields that are either completely irrotational or completely solenoidal. Since a static electric field is irrotational, we will use the symbol \mathbf{e} for an irrotational field. The symbol \mathbf{E} , often used for the field itself, will be reserved here for the Fourier transform of \mathbf{e} . Likewise, since a steady magnetic field is solenoidal, we will use the symbol \mathbf{b} for a solenoidal field and \mathbf{B} for its Fourier transform.

C. Previous Reconstruction Formulas

In [14], it was shown that if the total field is irrotational it can be reconstructed using only one set of probe measurements, and the reconstruction formula is

$$\psi = \mathcal{R}^* \mathcal{K}' \frac{g^{\mathbf{p}}}{\mathbf{p} \cdot \boldsymbol{\omega}}, \quad \mathbf{p} \cdot \boldsymbol{\omega} \neq 0 \quad (8a)$$

$$\mathbf{e} = \nabla \psi. \quad (8b)$$

If the field is known to be solenoidal, then two sets of probe measurements—using, say, probes \mathbf{p}_1 and \mathbf{p}_2 —are required. The reconstruction formula is

$$\mathbf{a} = \mathcal{R}^* \mathcal{K}' \begin{bmatrix} (\mathbf{p}_1 \times \boldsymbol{\omega})^T \\ (\mathbf{p}_2 \times \boldsymbol{\omega})^T \\ \boldsymbol{\omega}^T \end{bmatrix}^{-1} \begin{bmatrix} g^{\mathbf{p}_1} \\ g^{\mathbf{p}_2} \\ 0 \end{bmatrix} \quad (9a)$$

$$\mathbf{b} = \nabla \times \mathbf{a} \quad (9b)$$

where it is required that \mathbf{p}_1 , \mathbf{p}_2 , and $\boldsymbol{\omega}$ be linearly independent.

Note that these reconstruction formulas first reconstruct the respective potential functions and then take derivatives—gradient in the case of the irrotational field and curl in the case of the solenoidal field. Two pertinent comments follow from this observation. First, any information about the field derivable from a potential function can be extracted without reconstructing the full field. Second, these formulas are not convolution backprojection formulas since the gradient and curl operators represent an additional convolution after backprojection. Thus, the formulas (8a) and (9a) potentially provide shortcuts to the calculation of key field properties, while the completion of these formulas using derivatives in 3-D, represented by (8b) and (9b), are costly and potentially unstable ways to reconstruct the actual fields. This paper addresses this problem through the development of convolution backprojection formulas for \mathbf{e} and \mathbf{b} .

The irrotational and solenoidal components of an arbitrary field \mathbf{q} can be imaged separately and then added together to form the total field. The irrotational part is imaged using the probe $\boldsymbol{\omega}$; the solenoidal part is imaged using probes \mathbf{p}_1 and \mathbf{p}_2 , which are linearly independent and orthogonal to $\boldsymbol{\omega}$. With these probes, the reconstruction formulas given in (8a) and (9a) give the potential functions for the irrotational and solenoidal components of \mathbf{q} , respectively, and (8b) and (9b) give the components themselves.

III. PROJECTION THEOREMS AND RECONSTRUCTION FORMULAS

Use of the frequency domain has proven to be extremely important in the development of reconstruction formulas for projection imaging. In this section, we develop three new projection theorems for vector tomography. As in standard computed tomography, these theorems help both in understanding the action of the probe transform and in the development of new reconstruction formulas. It should be noted that two projection theorems for 2-D vector tomography have already been reported in the literature [6], [9], [18]. The results in this section extend the 2-D results of [9] to three dimensions.

A. Projection Theorems

The standard 3-D projection theorem (also called a projection-slice theorem or a central-slice theorem) relates the 1-D Fourier transform of a projection of f to a “central slice” of the 3-D Fourier transform of f . This theorem can be stated concisely [16] as

$$G(\rho, \boldsymbol{\omega}) = F(\rho\boldsymbol{\omega}) \quad (10)$$

where

$$F(\boldsymbol{\nu}) = \mathcal{F}_3\{f(\mathbf{x})\} = \int_{\mathbb{R}^3} f(\mathbf{x}) e^{-j2\pi\boldsymbol{\nu} \cdot \mathbf{x}} d\mathbf{x} \quad (11)$$

is the 3-D Fourier transform of f and

$$G(\rho, \boldsymbol{\omega}) = \mathcal{F}_1\{\tilde{f}(l, \boldsymbol{\omega})\} = \int_{\mathbb{R}^1} \tilde{f}(l, \boldsymbol{\omega}) e^{-j2\pi\rho l} dl \quad (12)$$

is the 1-D Fourier transform of $\tilde{f}(l, \boldsymbol{\omega})$. The well-known *Fourier reconstruction method* is based directly on this theorem; the *filtered backprojection* and *convolution backprojection* methods are readily derived from this theorem (cf., [16]).

A projection theorem for vector tomography is found by taking the 1-D Fourier transform of the probe transform (1). Accordingly, we get

$$\begin{aligned} G^{\mathbf{p}}(\rho, \boldsymbol{\omega}) &= \mathcal{F}_1\{g^{\mathbf{p}}(l, \boldsymbol{\omega})\} \\ &= \mathcal{F}_1\left\{\int_{\mathbb{R}^3} \mathbf{p}(l, \boldsymbol{\omega}) \cdot \mathbf{q}(\mathbf{x}) \delta(l - \boldsymbol{\omega} \cdot \mathbf{x}) d\mathbf{x}\right\} \\ &= \int_{\mathbb{R}^3} \int_{\mathbb{R}^1} \mathbf{p}(l, \boldsymbol{\omega}) \\ &\quad \cdot \mathbf{q}(\mathbf{x}) \delta(l - \boldsymbol{\omega} \cdot \mathbf{x}) e^{-j2\pi\rho l} dl d\mathbf{x} \\ &= \int_{\mathbb{R}^3} \mathbf{p}(\boldsymbol{\omega} \cdot \mathbf{x}, \boldsymbol{\omega}) \cdot \mathbf{q}(\mathbf{x}) e^{-j2\pi\rho\boldsymbol{\omega} \cdot \mathbf{x}} d\mathbf{x} \end{aligned} \quad (13)$$

where the final equation follows from the sifting property of the impulse function. This equation is recognized as a 3-D Fourier transform with the frequency variable $\boldsymbol{\nu} = \rho\boldsymbol{\omega}$. This leads to a the following very general vector projection theorem:

$$G^{\mathbf{p}}(\rho, \boldsymbol{\omega}) = \mathcal{F}_3\{\mathbf{p}(\boldsymbol{\omega} \cdot \mathbf{x}, \boldsymbol{\omega}) \cdot \mathbf{q}(\mathbf{x})\}_{\boldsymbol{\nu}=\rho\boldsymbol{\omega}}. \quad (14)$$

An important special case follows immediately by restricting the probe direction to depend only on $\boldsymbol{\omega}$ —i.e., the orientation of the planes of integration, not their spatial position. In this case $\mathbf{p}(l, \boldsymbol{\omega}) = \mathbf{p}(\boldsymbol{\omega})$, and it follows from (14) that

$$G^{\mathbf{p}}(\rho, \boldsymbol{\omega}) = \mathbf{p}(\boldsymbol{\omega}) \cdot \mathbf{Q}(\rho\boldsymbol{\omega}) \quad (15)$$

where \mathbf{Q} is the 3-D Fourier transform of \mathbf{q} .

Using (15) and the Helmholtz decomposition of \mathbf{q} leads to a very powerful projection theorem. Since $\mathbf{q} = \mathbf{q}_I + \mathbf{q}_S$ it follows that $\mathbf{Q} = \mathbf{Q}_I + \mathbf{Q}_S$, where \mathbf{Q}_I and \mathbf{Q}_S represent the 3-D Fourier transforms of the irrotational and solenoidal components of \mathbf{q} , respectively. It can be shown using well-known vector theorems that

$$\mathbf{Q}_I(\boldsymbol{\nu}) = j2\pi\boldsymbol{\nu}\Psi(\boldsymbol{\nu}) \quad (16a)$$

$$\mathbf{Q}_S(\boldsymbol{\nu}) = j2\pi\boldsymbol{\nu} \times \mathbf{A}(\boldsymbol{\nu}) \quad (16b)$$

where $\Psi(\boldsymbol{\nu}) = \mathcal{F}_3\{\psi(\mathbf{x})\}$ and $\mathbf{A}(\boldsymbol{\nu}) = \mathcal{F}_3\{\mathbf{a}(\mathbf{x})\}$. Therefore, from (15) it follows that

$$G^P(\rho, \boldsymbol{\omega}) = j2\pi\rho\{\mathbf{p}(\boldsymbol{\omega}) \cdot [\boldsymbol{\omega}\Psi(\rho\boldsymbol{\omega}) + \boldsymbol{\omega} \times \mathbf{A}(\rho\boldsymbol{\omega})]\} \quad (17)$$

which is a projection theorem relating the probe transform directly to the potential functions. This theorem is the starting point for the reconstruction formulas developed below. It should be noted that this theorem is completely general except that the probe direction is required to depend only on $\boldsymbol{\omega}$.

B. Reconstruction Formulas

We now use the projection theorem given in (17) to develop a collection of new reconstruction formulas. These formulas can also be derived from the results in [14]; but the overall approach here begins from first principles, not from existing formulas for the 3-D Radon transform.

1) *Irrotational Fields*: First, suppose that the total field \mathbf{e} is known to be irrotational. Then, since by assumption \mathbf{e} is zero on the boundary, $\mathbf{a} = 0$ and $\mathbf{A} = 0$. From (17) it follows that the Fourier transform of the scalar potential can be reconstructed using

$$\Psi(\rho\boldsymbol{\omega}) = \frac{G^P(\rho, \boldsymbol{\omega})}{j2\pi\rho[\mathbf{p}(\boldsymbol{\omega}) \cdot \boldsymbol{\omega}]} \quad (18)$$

provided that $\mathbf{p}(\boldsymbol{\omega}) \cdot \boldsymbol{\omega} \neq 0$. It follows that $\mathbf{e}(\mathbf{x})$ is given symbolically by

$$\mathbf{e}(\mathbf{x}) = \nabla \mathcal{F}_3^{-1}\{\Psi(\rho\boldsymbol{\omega})\}. \quad (19)$$

The actual implementation of this inverse Fourier transform requires some form of polar to rectangular coordinate transformation. One possibility is to interpolate the Fourier data given by $\Psi(\rho\boldsymbol{\omega})$ in polar coordinates onto a rectilinear grid; then take the inverse discrete Fourier transform. This approach is known in the classical CT literature as the Fourier method. Another approach is to write the inverse Fourier transform in polar coordinates and develop an analytic formula for inversion. We pursue this second approach now.

The inverse 3-D Fourier transform of $\Psi(\boldsymbol{\nu})$ is given by

$$\psi(\mathbf{x}) = \int_{\mathbb{R}^3} \Psi(\boldsymbol{\nu}) e^{j2\pi\boldsymbol{\nu} \cdot \mathbf{x}} d\boldsymbol{\nu}.$$

To relate this to the projection theorem (17) we make the substitution $\boldsymbol{\nu} = \rho\boldsymbol{\omega}$, where $-\infty < \rho < \infty$ and $\boldsymbol{\omega}$ ranges over half of the unit sphere, which we denote by \mathbb{H}^2 . Using this substitution it can be shown that

$$\psi(\mathbf{x}) = \int_{-\infty}^{\infty} \int_{\mathbb{H}^2} \rho^2 \Psi(\rho\boldsymbol{\omega}) e^{j2\pi\rho\boldsymbol{\omega} \cdot \mathbf{x}} d\boldsymbol{\omega} d\rho.$$

Taking the gradient of this expression and replacing $\Psi(\rho\boldsymbol{\omega})$ with the expression in (18) yields

$$\mathbf{e}(\mathbf{x}) = \int_{\mathbb{H}^2} \frac{\boldsymbol{\omega}}{\mathbf{p}(\boldsymbol{\omega}) \cdot \boldsymbol{\omega}} \int_{-\infty}^{\infty} \rho^2 G^P(\rho, \boldsymbol{\omega}) \cdot e^{j2\pi\rho\boldsymbol{\omega} \cdot \mathbf{x}} d\rho d\boldsymbol{\omega}. \quad (20)$$

From this expression and using the definition of the 1-D Fourier transform, it is straightforward to write both a filtered

backprojection formula

$$\mathbf{e}(\mathbf{x}) = \int_{\mathbb{H}^2} \frac{\boldsymbol{\omega}}{\mathbf{p}(\boldsymbol{\omega}) \cdot \boldsymbol{\omega}} \mathcal{F}_1^{-1}\{\rho^2 G^P(\rho, \boldsymbol{\omega})\}_{l=\boldsymbol{\omega} \cdot \mathbf{x}} d\boldsymbol{\omega} \quad (21)$$

and a convolution backprojection formula

$$\mathbf{e}(\mathbf{x}) = \frac{-1}{4\pi^2} \int_{\mathbb{H}^2} \frac{\boldsymbol{\omega}}{\mathbf{p}(\boldsymbol{\omega}) \cdot \boldsymbol{\omega}} g_{ll}^P(\boldsymbol{\omega} \cdot \mathbf{x}, \boldsymbol{\omega}) d\boldsymbol{\omega} \quad (22)$$

where the double subscript indicates second derivative with respect to l .

Equations (21) and (22) are new reconstruction formulas for irrotational fields given a single set of probe measurements where the probe depends only on $\boldsymbol{\omega}$. Two derivatives of each probe projection are required. In theory, this can either be accomplished by convolving the projection with a triplet or by filtering it with a rho-squared filter. This filtered projection is backprojected into \mathbb{R}^3 by substituting $\boldsymbol{\omega} \cdot \mathbf{x}$ for l . Next, a weight is applied to the backprojection function according to its backprojection orientation, and these weighted backprojection functions are integrated to produce a reconstructed irrotational field. Comparing (22) to a standard 3-D reconstruction formula for scalar functions (cf., [19]) reveals only one key difference: the weighting $\boldsymbol{\omega}/\mathbf{p}(\boldsymbol{\omega}) \cdot \boldsymbol{\omega}$. This is a very minor difference which does not affect the overall computational complexity of the reconstruction algorithm. Thus, reconstructing an irrotational vector field from its 3-D probe transform has the same fundamental complexity as reconstructing a scalar field from its 3-D Radon transform.

2) *Solenoidal Fields*: If the total field \mathbf{b} is solenoidal, then $\Psi(\boldsymbol{\nu}) = 0$ (since \mathbf{b} is zero on the boundary). From (17), it follows that

$$\begin{aligned} G^P(\rho, \boldsymbol{\omega}) &= (j2\pi\rho)\mathbf{p}(\boldsymbol{\omega}) \cdot [\boldsymbol{\omega} \times \mathbf{A}(\rho\boldsymbol{\omega})] \\ &= (j2\pi\rho)\mathbf{A}(\rho\boldsymbol{\omega}) \cdot [\mathbf{p}(\boldsymbol{\omega}) \times \boldsymbol{\omega}] \end{aligned} \quad (23)$$

where the second equality follows from a basic property of the triple product. From Helmholtz's theorem, we know that the vector potential is solenoidal—i.e., $\nabla \cdot \mathbf{a}(\mathbf{x}) = 0$ —which implies

$$(j2\pi\rho)[\mathbf{A}(\rho\boldsymbol{\omega}) \cdot \boldsymbol{\omega}] = 0.$$

Putting this equation together with (23) for two probes $\mathbf{p}_1(\boldsymbol{\omega})$ and $\mathbf{p}_2(\boldsymbol{\omega})$ yields the system

$$\begin{bmatrix} G^{\mathbf{p}_1}(\rho, \boldsymbol{\omega}) \\ G^{\mathbf{p}_2}(\rho, \boldsymbol{\omega}) \\ 0 \end{bmatrix} = (j2\pi\rho) \begin{bmatrix} [\mathbf{p}_1(\boldsymbol{\omega}) \times \boldsymbol{\omega}]^T \\ [\mathbf{p}_2(\boldsymbol{\omega}) \times \boldsymbol{\omega}]^T \\ \boldsymbol{\omega}^T \end{bmatrix} \mathbf{A}(\rho\boldsymbol{\omega}).$$

If $\mathbf{p}_1(\boldsymbol{\omega})$ and $\mathbf{p}_2(\boldsymbol{\omega})$ are chosen so that $\{\mathbf{p}_1(\boldsymbol{\omega}), \mathbf{p}_2(\boldsymbol{\omega}), \boldsymbol{\omega}\}$ are linearly independent, then

$$\mathbf{A}(\rho\boldsymbol{\omega}) = (j2\pi\rho)^{-1} \begin{bmatrix} [\mathbf{p}_1(\boldsymbol{\omega}) \times \boldsymbol{\omega}]^T \\ [\mathbf{p}_2(\boldsymbol{\omega}) \times \boldsymbol{\omega}]^T \\ \boldsymbol{\omega}^T \end{bmatrix}^{-1} \begin{bmatrix} G^{\mathbf{p}_1}(\rho, \boldsymbol{\omega}) \\ G^{\mathbf{p}_2}(\rho, \boldsymbol{\omega}) \\ 0 \end{bmatrix} \quad (24)$$

and $\mathbf{b}(\mathbf{x})$ is given symbolically by

$$\mathbf{b}(\mathbf{x}) = \nabla \times \mathcal{F}_3^{-1}\{\mathbf{A}(\rho\boldsymbol{\omega})\}. \quad (25)$$

The same considerations regarding polar-to-rectangular conversion as in irrotational fields must be made here. Direct

interpolation onto a rectangular lattice of the known values of $\mathbf{A}(\rho\omega)$ yields a Fourier reconstruction method. Alternatively, writing the inverse transform in polar coordinates yields direct filtered backprojection and convolution backprojection formulas. Following steps analogous to the irrotational case, we first write

$$\mathbf{a}(\mathbf{x}) = \int_{\mathbb{R}^3} \mathbf{A}(\nu) e^{j2\pi\nu\cdot\mathbf{x}} d\nu$$

which leads to the polar form

$$\mathbf{a}(\mathbf{x}) = \int_{-\infty}^{\infty} \int_{\mathbb{H}^2} \rho^2 \mathbf{A}(\rho\omega) e^{j2\pi\rho\omega\cdot\mathbf{x}} d\omega d\rho.$$

Taking the curl of this and manipulating the resulting expression yields

$$\mathbf{b}(\mathbf{x}) = \int_{\mathbb{H}^2} \omega \times \int_{-\infty}^{\infty} j2\pi\rho^3 \mathbf{A}(\rho\omega) e^{j2\pi\rho\omega\cdot\mathbf{x}} d\rho d\omega. \quad (26)$$

To further simplify this, we let

$$\mathbf{P}(\omega) = \begin{bmatrix} [\mathbf{p}_1(\omega) \times \omega]^T \\ [\mathbf{p}_2(\omega) \times \omega]^T \\ \omega^T \end{bmatrix}$$

and

$$\mathbf{G}(\rho, \omega) = \begin{bmatrix} G^{\mathbf{p}_1}(\rho, \omega) \\ G^{\mathbf{p}_2}(\rho, \omega) \\ 0 \end{bmatrix}$$

and use (24), yielding after some simplification

$$\mathbf{b}(\mathbf{x}) = \int_{\mathbb{H}^2} \omega \times \mathbf{P}^{-1}(\omega) \cdot \int_{-\infty}^{\infty} \rho^2 \mathbf{G}(\rho, \omega) e^{j2\pi\rho\omega\cdot\mathbf{x}} d\rho d\omega. \quad (27)$$

This equation can be put into the form of a filtered backprojection formula

$$\mathbf{b}(\mathbf{x}) = \int_{\mathbb{H}^2} \omega \times \mathbf{P}^{-1}(\omega) \mathcal{F}_1^{-1} \{ \rho^2 \mathbf{G}(\rho, \omega) \}_{t=\omega\cdot\mathbf{x}} d\omega \quad (28)$$

and a convolution backprojection formula

$$\mathbf{b}(\mathbf{x}) = \frac{-1}{4\pi^2} \int_{\mathbb{H}^2} \omega \times \mathbf{P}^{-1}(\omega) \mathbf{g}_{ll}(\omega \cdot \mathbf{x}, \omega) d\omega \quad (29)$$

where $\mathbf{g}(l, \omega) = \mathcal{F}_1^{-1} \{ \mathbf{G}(\rho, \omega) \}$. Once again, the convolution kernel turns out to be just the second derivative operator. As in the irrotational case, the filtered projections are backprojected, weighted, and integrated to form the reconstructed vector field. Note that although \mathbf{g} is a 3-D vector, only two of its components are nonzero; therefore, only two probe transforms, $g^{\mathbf{p}_1}$ and $g^{\mathbf{p}_2}$, are required to reconstruct a solenoidal field.

3) *Arbitrary Vector Fields*: It follows from (17) that the components \mathbf{q}_I and \mathbf{q}_S of an arbitrary vector field \mathbf{q} can be imaged separately. In particular, if $\mathbf{p}(\omega) = \omega$, then since $\omega \times \omega = 0$, the solenoidal component of the field is invisible. Therefore, for $\mathbf{p}(\omega) = \omega$ any of the reconstruction formulas for an irrotational field can be used directly to reconstruct the irrotational component \mathbf{q}_I . For example, from (22) we see that

the irrotational component of an arbitrary vector field is given by

$$\mathbf{q}_I(\mathbf{x}) = \frac{-1}{4\pi^2} \int_{\mathbb{H}^2} \omega g_{ll}^{\omega}(\omega \cdot \mathbf{x}, \omega) d\omega. \quad (30)$$

In similar fashion, we see from (17) that the irrotational part of the field is invisible if $\mathbf{p}(\omega)$ is orthogonal to ω . Since the linear subspace orthogonal to ω is 2-D, two probes \mathbf{p}_1 and \mathbf{p}_2 can be selected that are linearly independent and orthogonal to ω . Accordingly, any of the reconstruction formulas for a solenoidal field can be used to reconstruct the solenoidal component of an arbitrary vector field. A simpler formula can be derived, however, by noting that when \mathbf{p}_1 and \mathbf{p}_2 are orthogonal to ω , it follows that

$$\mathbf{P}^{-1}(\omega) = \begin{bmatrix} \frac{\mathbf{p}_2}{[\mathbf{p}_2 \mathbf{p}_1 \omega]} & \frac{\mathbf{p}_1}{[\mathbf{p}_1 \mathbf{p}_2 \omega]} & \omega \end{bmatrix}$$

where the notation $[\mathbf{abc}]$ is standard for triple product and is equal to $\mathbf{a} \cdot (\mathbf{b} \times \mathbf{c})$. The cross product $\omega \times \mathbf{P}^{-1}$ appearing in (29) simplifies since $\omega \times \omega = 0$, and the equation can be put into the form

$$\mathbf{q}_S(\mathbf{x}) = \frac{-1}{4\pi^2} \int_{\mathbb{H}^2} \begin{bmatrix} \frac{\omega \times \mathbf{p}_2}{[\mathbf{p}_2 \mathbf{p}_1 \omega]} & \frac{\omega \times \mathbf{p}_1}{[\mathbf{p}_1 \mathbf{p}_2 \omega]} \\ g_{ll}^{\mathbf{p}_1}(\omega \cdot \mathbf{x}, \omega) \\ g_{ll}^{\mathbf{p}_2}(\omega \cdot \mathbf{x}, \omega) \end{bmatrix} d\omega. \quad (31)$$

An even simpler equation results if $\{\mathbf{p}_1, \mathbf{p}_2, \omega\}$ form a right-handed orthonormal basis. In this case it is easy to verify that

$$\mathbf{q}_S(\mathbf{x}) = \frac{-1}{4\pi^2} \int_{\mathbb{H}^2} [\mathbf{p}_1 \quad \mathbf{p}_2] \begin{bmatrix} g_{ll}^{\mathbf{p}_1}(\omega \cdot \mathbf{x}, \omega) \\ g_{ll}^{\mathbf{p}_2}(\omega \cdot \mathbf{x}, \omega) \end{bmatrix} d\omega. \quad (32)$$

Two equations, (30) and either (31) or (32), can be now used to independently image and reconstruct the irrotational and solenoidal components of an arbitrary field. These equations can also be put together to give a single formula for reconstructing the total field. Assuming $\{\mathbf{p}_1, \mathbf{p}_2, \omega\}$ form a right-handed orthonormal basis, (30) and (32) give

$$\mathbf{q}(\mathbf{x}) = \frac{-1}{4\pi^2} \int_{\mathbb{H}^2} \mathbf{p}_1(\omega) g_{ll}^{\mathbf{p}_1}(\omega \cdot \mathbf{x}, \omega) + \mathbf{p}_2(\omega) g_{ll}^{\mathbf{p}_2}(\omega \cdot \mathbf{x}, \omega) + \omega g_{ll}^{\omega}(\omega \cdot \mathbf{x}, \omega) d\omega \quad (33)$$

which is a remarkably simple formula for reconstructing a vector field from its probe transform measurements.

IV. SIMULATION RESULTS

A. Full 3-D Reconstructions

Three vector fields were defined on the unit cube ($-1 \leq x, y, z \leq 1$) and sampled on a 16^3 lattice. The continuous fields are all from the space \mathcal{D} , with support on the unit sphere. The small lattice size was used both to reduce computation time and to improve visualization of the results. The first field is irrotational, the second is solenoidal, and the third is the

sum of these two. The scalar and vector potentials

$$\psi(\mathbf{x}) = \begin{cases} \frac{1}{2} \exp\left(\frac{-1}{1-|\mathbf{x}|^2}\right), & |\mathbf{x}| < 1 \\ 0, & \text{otherwise} \end{cases} \quad (34)$$

$$\mathbf{a}(\mathbf{x}) = \begin{cases} \exp\left(\frac{-1}{1-|\mathbf{x}|^2}\right) \begin{bmatrix} -y \\ x \\ 0 \end{bmatrix}, & |\mathbf{x}| < 1 \\ 0, & \text{otherwise} \end{cases} \quad (35)$$

where $|\mathbf{x}| = \sqrt{x^2 + y^2 + z^2}$ are used to define the irrotational and solenoidal fields

$$\mathbf{e}(\mathbf{x}) = \nabla\psi(\mathbf{x}) = \begin{cases} \frac{-1}{(1-|\mathbf{x}|^2)^2} \exp\left(\frac{-1}{1-|\mathbf{x}|^2}\right) \begin{bmatrix} x \\ y \\ z \end{bmatrix}, & |\mathbf{x}| < 1 \\ 0, & \text{otherwise} \end{cases} \quad (36)$$

$$\mathbf{b}(\mathbf{x}) = \nabla \times \mathbf{a}(\mathbf{x}) = \begin{cases} 2 \exp\left(\frac{-1}{1-|\mathbf{x}|^2}\right) \begin{bmatrix} \frac{xz}{(1-|\mathbf{x}|^2)^2} \\ \frac{yz}{(1-|\mathbf{x}|^2)^2} \\ 1 - \frac{x^2 + y^2}{(1-|\mathbf{x}|^2)^2} \end{bmatrix}, & |\mathbf{x}| < 1 \\ 0, & \text{otherwise.} \end{cases} \quad (37)$$

Assigning $\mathbf{q}_I = \mathbf{e}$ and $\mathbf{q}_S = \mathbf{b}$ gives a third vector field

$$\mathbf{q}(\mathbf{x}) = \mathbf{e}(\mathbf{x}) + \mathbf{b}(\mathbf{x}) \quad (38)$$

which obviously has both irrotational and solenoidal components. Also, it is readily verified that $\nabla \times \mathbf{e} = 0$, $\nabla \cdot \mathbf{a} = 0$, and $\nabla \cdot \mathbf{b} = 0$.

All five fields— ψ , \mathbf{a} , \mathbf{e} , \mathbf{b} , and \mathbf{q} —are shown in Fig. 1. By design, the magnitudes of all five fields are zero on the boundary of the cube and larger near the center. The value of the scalar potential ψ , shown in Fig. 1(a), is proportional to the diameter of the ball. The corresponding irrotational field \mathbf{e} , shown in Fig. 1(c), shows vectors pointing toward the origin, implying the existence of a sink at the origin. Note that the magnitude of these vectors is largest on a shell enclosing the origin. There is, of course, no rotation (curl or vorticity) in this field. The vector potential \mathbf{a} , shown in Fig. 1(b), shows a 2-D circulation around one axis. It is not surprising that this field would demonstrate this type of circulation, since we know that the vector potential is itself solenoidal. The corresponding solenoidal field \mathbf{b} , shown in Fig. 1(d), demonstrates a more complicated circulation through and around the origin. This field has no divergence; therefore, no particles moving through this field could either be lost from the cube or emanate from or converge to a point. The total field \mathbf{q} , shown in Fig. 1(e), shows evidence of both field components—some convergence toward the origin and some swirling through and around the origin.

The probe transforms of the three fields \mathbf{e} , \mathbf{b} , and \mathbf{q} were computed numerically as follows. Fifty-four orientations of $\boldsymbol{\omega}$ were chosen to sample the top half of the unit sphere

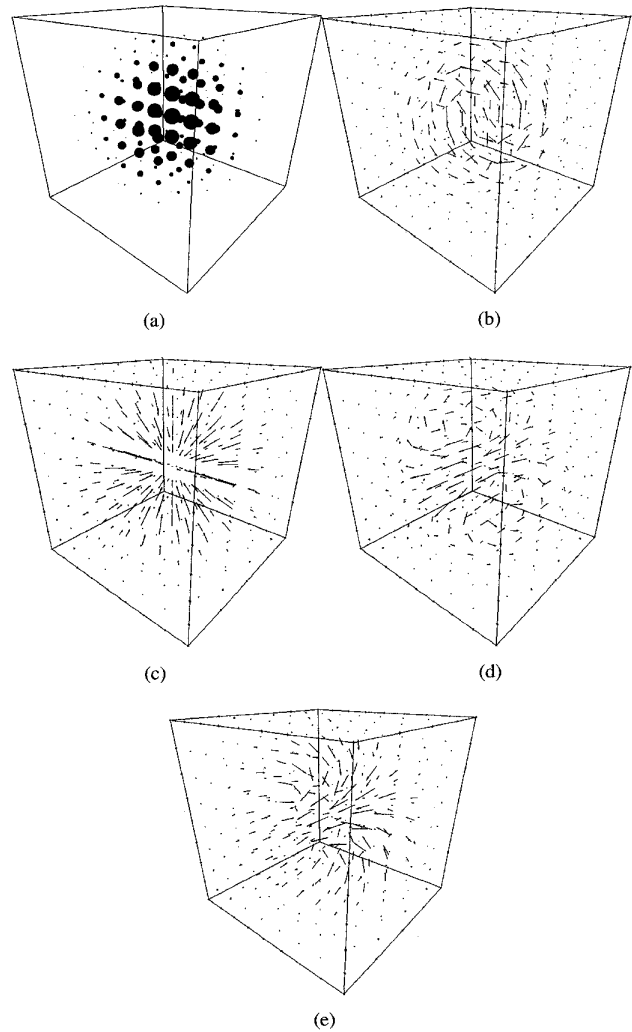


Fig. 1. Simulated potentials and fields. (a) Scalar potential ψ . (b) Vector potential \mathbf{a} . (c) Irrotational field \mathbf{e} . (d) Solenoidal field \mathbf{b} . (e) Total field \mathbf{q} .

with nearly equal areas. Fig. 2 gives a view of the top of the unit sphere indicating the placement of these 54 samples. The ordering from 1–54 is shown primarily to make it easier to display the acquired data (see below); however, it also suggests that a spiral is one possible way to generate $\boldsymbol{\omega}$ -samples in practice. Given the elevation and azimuth angles of an $\boldsymbol{\omega}$ sample, a Euler matrix was constructed to rotate the unit vector pointing in the $+z$ direction directly to $\boldsymbol{\omega}$. The probe vectors \mathbf{p}_1 and \mathbf{p}_2 were generated by applying this same Euler matrix to the unit vectors pointing in the $+x$ and $+y$ directions, respectively. The resultant set of probes $\{\mathbf{p}_1, \mathbf{p}_2, \boldsymbol{\omega}\}$ is a right-handed orthonormal basis. A different right-handed orthonormal basis is generated for each of the 54 samples $\boldsymbol{\omega}_i$, $i = 1, \dots, 54$.

Given a direction $\boldsymbol{\omega}_i$, three planar integrals approximating (1) for each of the three probes \mathbf{p}_1 , \mathbf{p}_2 , and $\boldsymbol{\omega}_i$ were numerically calculated at 29 evenly spaced lateral positions l_j , $j = 1, \dots, 29$. For a particular pair $(l_j, \boldsymbol{\omega}_i)$, three scalar fields were created by taking the inner product of the three probes with the vector field on the plane $L(l_j, \boldsymbol{\omega}_i) = \{\mathbf{x} | l_j = \boldsymbol{\omega}_i \cdot \mathbf{x}\}$. Each

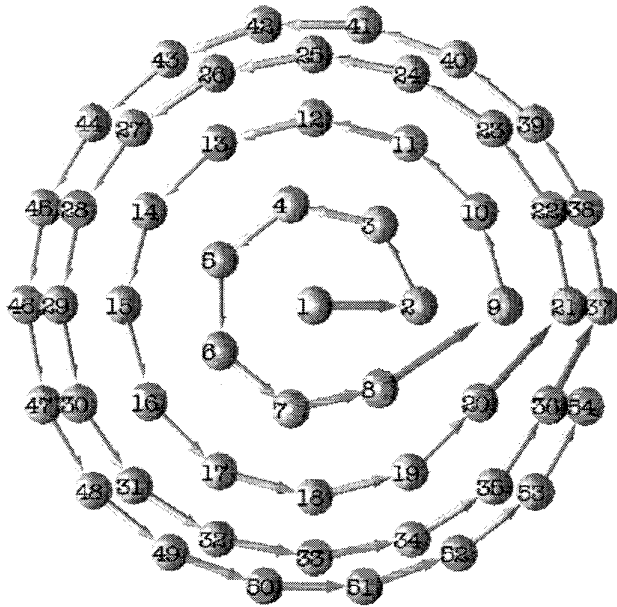


Fig. 2. Positions of ω -samples looking at the unit sphere from the top.

field was then numerically integrated by sampling the plane using 32^2 samples on a square section of the plane covering the unit sphere. Trilinear interpolation was used to determine the value of a vector field for sample points not falling on a lattice point.

Sinograms representing the probe transforms are shown in Fig. 3. Each row of a sinogram corresponds to a given ω_i , $i = 1, \dots, 54$, where the top row corresponds to ω_1 and the bottom row to ω_{54} . The columns correspond to the lateral displacements l_j , $j = 1, \dots, 29$, with the center column corresponding to integration through the origin. Thus, a row of a sinogram is a projection, and there are 54 projections. Alternately, a sinogram can be viewed as a gray-scale representation of the matrix $[g^P(l_j, \omega_i)]$ where i indexes the rows and j indexes the columns. Note that there is a periodicity reflected in the sinograms of p_1 and p_2 . This periodicity has an increasing period from top to bottom because there are more samples around the unit sphere at the equator. This sampling strategy is necessary to give nearly equal-area sampling of the sphere. Also note that two of the sinograms of e are nearly zero (a neutral gray color is zero) because irrotational fields are invisible to probes orthogonal to ω . Similarly, one of the sinograms of b is nearly zero because solenoidal fields are invisible to probes parallel to ω . The nonzero sinograms of e and b agree to good approximation with those of q , indicating that the probes can separate the components of an arbitrary field quite well.

We now focus on reconstructing the potentials and fields from the probe transform measurements of the total field q ; thus, we reconstruct from the sinograms on the bottom row of Fig. 3. The scalar and vector potential fields were reconstructed using discrete approximations to (8) and (9), respectively. The irrotational and solenoidal components and the full field were reconstructed using discrete approximations

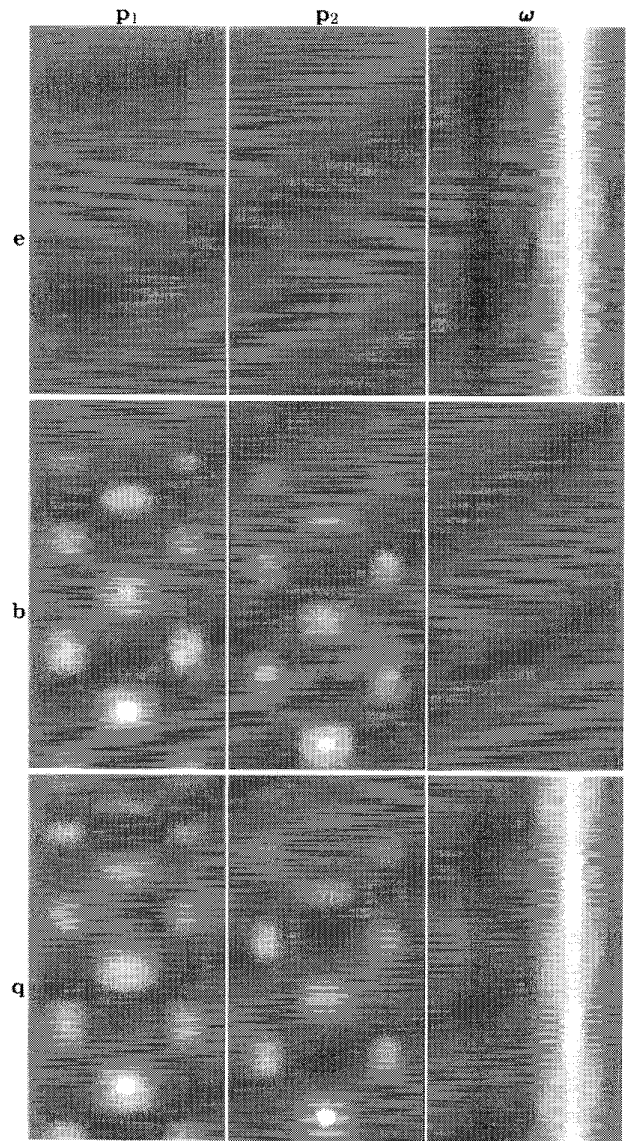


Fig. 3. Sinograms of the probe transforms of the irrotational field e (top row), the solenoidal field b (middle row), and the total field q (bottom row).

to (22), (32), and (33), respectively. These discrete approximations used central differences to approximate derivatives and replaced the backprojection integral with a summation in which the samples were weighted by the areas accorded to each angular sample. These reconstructions are shown in Fig. 4. Note that the respective fields appearing in Figs. 1 and 4 are plotted using the same scale, so visual comparison is meaningful (however, different fields are scaled differently so that at least some detail within each field is visible). The error is very small despite the relative sparsity of data; it is, in fact, difficult to see any difference between the reconstructions and the truth. A plot of the error vectors shown on the same scale as the truth has vectors so small that little qualitative information is available. In a more detailed comparison, however, we have observed that the reconstructed vectors are somewhat too short on average, and the orientations of the largest vectors are very

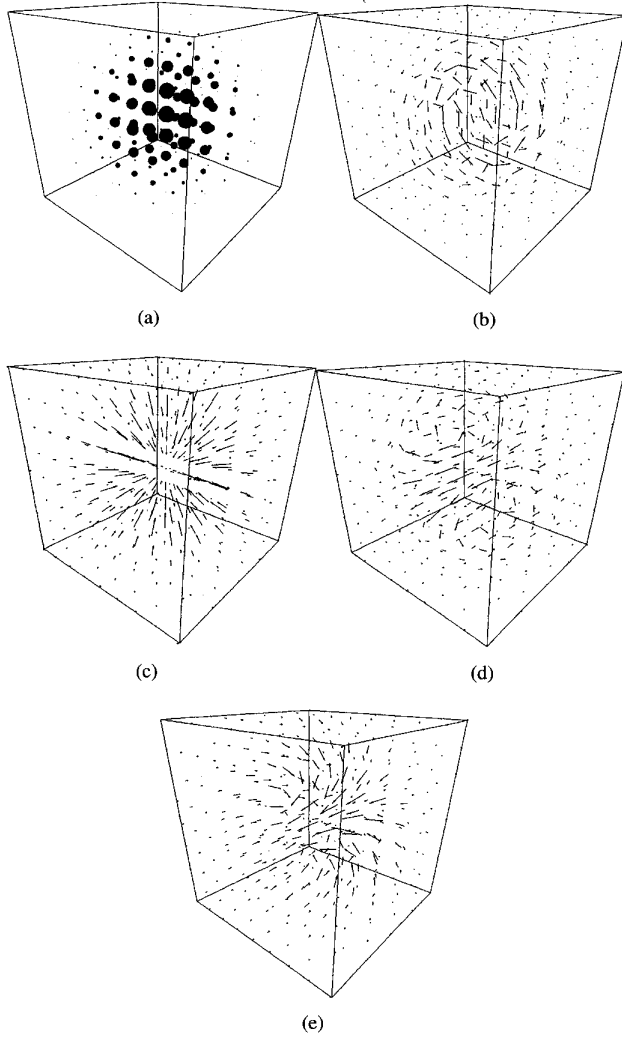


Fig. 4. Reconstructed potentials and fields. (a) Scalar potential ψ . (b) Vector potential \mathbf{a} . (c) Irrotational field \mathbf{e} . (d) Solenoidal field \mathbf{b} (e) Total field \mathbf{q} .

nearly exact.

Quantitative results for reconstructing the potentials and fields are given in Table I. This table gives average errors for simulations in which the source fields were purely irrotational, purely solenoidal, and the sum of these two. Since it is not possible to reconstruct \mathbf{a} , \mathbf{b} , and \mathbf{q} from \mathbf{e} alone or ψ , \mathbf{e} , and \mathbf{q} from \mathbf{b} alone, these entries are denoted n/a for “not applicable.” All remaining boxes contain a number in the leftmost part, which gives the square root of the average squared error—i.e., the root mean square error (RMSE), defined as

$$\text{RMSE} = \sqrt{\frac{1}{N} \sum_{i=1}^N |\mathbf{q}_i - \hat{\mathbf{q}}_i|^2}$$

where N is the number of lattice points in the unit sphere. The boxes corresponding to the reconstruction of vector fields (including \mathbf{a}) have two additional numbers corresponding to average percent magnitude error and average angular error. For reference when discussing the RMSE, Table II gives the ranges and average values of the magnitude of the true fields.

TABLE I
AVERAGE RECONSTRUCTION ERRORS

	Source Field								
	\mathbf{e}			\mathbf{b}			\mathbf{q}		
ψ	0.364	-	-	n/a	-	-	0.367	-	-
$\hat{\mathbf{a}}$	n/a	-	-	0.539	11.9%	0.95°	0.541	11.9%	1.13°
$\hat{\mathbf{e}}$	3.471	-5.94%	0.96°	n/a	-	-	3.620	-5.87%	1.93°
$\hat{\mathbf{b}}$	n/a	-	-	5.733	-12.4%	3.53°	5.800	-12.3%	3.94°
$\hat{\mathbf{q}}$	n/a	-	-	n/a	-	-	6.574	-9.06%	4.42°

(Note: RMSE figures must be multiplied by 10^{-2})

TABLE II
RANGES AND AVERAGES OF THE MAGNITUDE OF THE TRUE FIELDS

	Minimum	Maximum	Average
ψ	0.00376	0.181	0.070
\mathbf{a}	0.00146	0.131	0.061
\mathbf{e}	0.00430	0.399	0.291
\mathbf{b}	0.05121	0.719	0.336
\mathbf{q}	0.01953	0.776	0.444

The RMSE captures the performance of each reconstruction in a single number. Since the RMSE values in Table I have the same units as the entries in corresponding rows in Table II, we can think of RMSE as an average deviation from the truth in the same physical units as the field being measured. Overall, the RMSE's are less than 18% of the average magnitude of their corresponding true fields and less than 9% of the maximum magnitude. These RMSE values also indicate that the presence of an “interfering” field only very slightly degrades our ability to extract a given potential or field component. For example, the presence of the solenoidal field \mathbf{b} causes the RMSE for reconstructing ψ to go up from 0.364×10^{-2} to 0.367×10^{-2} , less than a 1% change in the RMSE. Percent magnitude error or angular deviation is another indicator of the performance in reconstructing vector fields; these measures have the advantage of separating out quantities that may be of particular interest in a given application. From Table I we see that all field reconstructions in this simulation— $\hat{\mathbf{e}}$, $\hat{\mathbf{b}}$, and $\hat{\mathbf{q}}$ —have vectors that are, on average, too short; interestingly, reconstructing from the total field tended to reduce this error. The angular error in these same reconstructions, however, shows the exact reverse effect—i.e., the direction of a field component is better reconstructed from measurements of the field component by itself.

B. Local Reconstruction

Consider reconstructing the field \mathbf{q} at the point \mathbf{x}_0 using (33). All that is required are second derivatives (with respect to l) of the probe transforms g^{P_1} , g^{P_2} , and g^ω at the point $l_0 = \omega \cdot \mathbf{x}_0$ for all ω . This property is called *local reconstruction*, a property inherited from the Radon transform, where it is known that the inverse Radon transform operator is local in odd dimensions [20]. Thus, in 3-D vector tomography it is theoretically possible to reconstruct a vector at \mathbf{x}_0 given only measurements on planes passing through \mathbf{x}_0 . In practice, two approximations must be made in order to compute the required derivatives. First, since ω is sampled, the integral

TABLE III
LOCAL RECONSTRUCTION ERROR ($\times 10^{-2}$)

Number of Angles, M	Plane Spacing, T									
	0.04	0.08	0.12	0.16	0.20	0.24	0.28	0.32	0.36	0.40
54	3.14	2.22	1.83	1.45	1.46	1.69	2.19	2.88	3.61	4.36
147	1.81	1.79	1.74	1.68	1.75	2.08	2.57	3.14	3.76	4.39
233	3.66	3.64	3.13	2.49	2.20	2.21	2.46	2.94	3.51	4.15
341	0.81	0.78	1.06	1.41	1.81	2.23	2.69	3.14	3.63	4.19
540	0.28	0.65	1.02	1.40	1.82	2.25	2.67	3.10	3.59	4.17
976	0.99	0.79	0.96	1.39	1.84	2.23	2.63	3.08	3.58	4.16
1537	0.46	0.63	1.02	1.43	1.82	2.23	2.63	3.07	3.56	4.15
2224	0.43	0.60	1.03	1.42	1.82	2.23	2.63	3.06	3.56	4.14
3221	0.24	0.64	1.03	1.42	1.81	2.22	2.62	3.05	3.55	4.13

in (33) must be approximated by a sum. Second, since l is sampled, the second derivatives in (33) must be calculated by finite differences. Still, an experiment designed to reconstruct only $\mathbf{q}(\mathbf{x}_0)$ would require only three plane integrals for each ω , provided that those planes could be positioned precisely. A retrospective experiment (or one that allows only coarse placement of the planes) would require at least four plane integral measurements for each ω to allow for interpolation of the second derivatives. In our simulations we used a combination of the two schemes: four plane integrals per ω were used, where the four planes were equally spaced and centered at l_0 . Central differences were used to approximate the two derivatives, and linear interpolation was then used to determine the second derivatives at l_0 .

Given the above scenario, the remaining free parameters in a local reconstruction experiment are the number of angles M and the spacing T between the planes. To study the relationship between these parameters and the reconstruction accuracy, we simulated noise-free local measurements of \mathbf{q} [see (38)] for many pairs (M, T) . The arrangement of the M angles was chosen to sample the halfsphere with nearly equal-area samples. For each ω , the lateral positions of four planes were centered at $l_0 = \omega \cdot \mathbf{x}_0$ where $\mathbf{x}_0 = (0.066\ 666\ 7, 0.066\ 666\ 7, 0.066\ 666\ 7)$ and were separated by T . The field was reconstructed using a numerical approximation to (33) in which the integral was replaced by a summation (weighted by the areas accorded to each angular sample) and the derivatives were approximated by central differences as described above. The resultant errors—that is, $|\hat{\mathbf{q}}(\mathbf{x}_0) - \mathbf{q}(\mathbf{x}_0)|$ —are shown in Table III.

The local reconstruction errors shown in Table III reveal several interesting properties. First, when the planes are far apart—i.e., T is large—the error is very large and largely independent of the number of angles. This indicates that for large T the derivative calculations are largely erroneous and cannot be corrected by taking more angles. Second, for smaller fixed T , increasing the number of angles reduces the error, although the effect is relatively small. Third, except for the region in which both M and T are small, the error decreases strongly with decreasing plane spacing. Finally, there is a clear anomalous behavior for small M and T . At this time, we have no conclusive explanation for the anomalous region. We speculate that the sampled angles are not sufficient in number nor suitably oriented to capture the true field at that point—i.e., that this is a type of aliasing phenomenon related to the interaction of sampling grids. Thus, except for this anomalous region, we can conclude that performance is improved by

taking more angles and moving the imaging planes closer together. In particular, for the M and T pair closest to that of our previous full reconstruction simulation ($M = 54$ and $T = 0.08$), the particular error here is 2.22×10^{-2} , about three times smaller than RMSE of 6.574×10^{-2} in Table I. From Table III, we see that it is possible to reduce this particular error by almost a factor of 10 (to 0.24×10^{-2} when $M = 3221$ and $T = 0.04$), which by analogy would reduce the average error to below 2% of the average field value.

V. APPLICATION TO MRI

Under a small phase-angle approximation (explained below), the 3-D probe transform of a vector field can be measured for arbitrary probe directions using magnetic resonance imaging (MRI) methods. It requires blending two imaging approaches: 3-D planar imaging [21] and phase-contrast imaging [22]. 3-D planar imaging uses a single 90° radio frequency pulse to excite the entire sample followed by a constant gradient during which the free induction decay (FID) is recorded. An echo can be employed to refocus the FID. The gradient direction during readout determines the direction ω ; the readout signal gives a series of planar integrals at different positions. To make these integrals sensitive to velocity, the gradient waveforms are manipulated before readout to provide first a velocity-nulled readout and then a velocity-sensitized readout. The three components of the probe vector are given by the first moments of the gradient waveforms. Taking the difference between these readouts gives a signal that, under a small phase-angle approximation, is a 3-D probe transform with a completely arbitrary probe direction. We now give a brief mathematical treatment of this new imaging approach.

After a nonselective 90° pulse, the FID is given to good approximation [23] by

$$s(t) = \iint \rho(\mathbf{x}, \mathbf{v}) e^{i\gamma[\mathbf{x} \cdot \mathbf{M}_0(t) + \mathbf{v} \cdot \mathbf{M}_1(t)]} d\mathbf{x} d\mathbf{v} \quad (39)$$

where $\rho(\mathbf{x}, \mathbf{v})$ represents spin density as a function of spatial position \mathbf{x} and velocity \mathbf{v} and

$$\begin{aligned} \mathbf{M}_0(t) &= \int_0^t \mathbf{G}(\tau) d\tau \\ \mathbf{M}_1(t) &= \int_0^t \tau \mathbf{G}(\tau) d\tau \end{aligned}$$

are the zeroth and first moments of the gradient waveform $\mathbf{G}(t)$. Making the assumption that at any given spatial position the velocity takes on only one value, we have $\rho(\mathbf{x}, \mathbf{v}) = \rho(\mathbf{x})\delta(\mathbf{v} - \mathbf{v}(\mathbf{x}))$. After the 90° pulse, the x , y , and z gradients are manipulated twice in order to achieve both velocity encoding and planar imaging. The first manipulation is the combined application of a dephasing pulse and a bipolar flow-encoding gradient pulse (cf., [24]), applied to all three gradients. This independently sets the zeroth and first moments of the gradient waveform. Next, a 180° radio frequency pulse is applied in order to generate a spin-echo [although a gradient echo could also be used (cf., [25])]. At time $t = t_r$, just prior to the echo, the gradients are set to constant values, represented by the readout gradient vector \mathbf{G}_r .

Choosing $\mathbf{M}_0(t_r) = \mathbf{G}_r t_r$ (using the dephasing pulse) yields the following signal during readout

$$s(t) = \int \rho(\mathbf{x}) e^{j\gamma \mathbf{x} \cdot \mathbf{G}_r t} e^{j\gamma \mathbf{v}(\mathbf{x}) \cdot (\mathbf{M}_1' + \mathbf{G}_r t^2/2)} d\mathbf{x} \quad (40)$$

where $\mathbf{M}_1' = \mathbf{M}_1(t_r) - \mathbf{G}_r t_r^2/2$ (set by the bipolar pulse). Now let $\boldsymbol{\omega} = \mathbf{G}_r/|\mathbf{G}_r|$ and $\mathbf{p}(\boldsymbol{\omega}) = \gamma \mathbf{M}_1'$. These vectors represent the unit normal and probe directions, respectively, and are completely arbitrary and user programmable. Taking the Fourier transform $S(f) = \mathcal{F}\{s(t)\}$ and defining

$$z(l, \boldsymbol{\omega}) = \frac{\gamma |\mathbf{G}_r|}{2\pi} S\left(\frac{\gamma |\mathbf{G}_r| l}{2\pi}\right) \quad (41)$$

gives

$$z(l, \boldsymbol{\omega}) = \int \rho(\mathbf{x}) e^{j\mathbf{p}(\boldsymbol{\omega}) \cdot \mathbf{v}(\mathbf{x})} \cdot \left[\sqrt{\frac{j\pi}{\beta'}} e^{-j\pi^2(l - \mathbf{x} \cdot \boldsymbol{\omega})^2/\beta'} \right] d\mathbf{x} \quad (42)$$

where $\beta' = 2\pi^2 \mathbf{v}(\mathbf{x}) \cdot \boldsymbol{\omega} / \gamma |\mathbf{G}_r|$. When β' is small enough, which can be assured by choosing $|\mathbf{G}_r|$ large enough, the bracketed term in the integrand above behaves like an impulse function. Therefore, we have the approximation

$$z(l, \boldsymbol{\omega}) = \int \rho(\mathbf{x}) e^{j\mathbf{p}(\boldsymbol{\omega}) \cdot \mathbf{v}(\mathbf{x})} \delta(l - \mathbf{x} \cdot \boldsymbol{\omega}) d\mathbf{x}. \quad (43)$$

When this approximation is not valid—either because of large velocities or small readout gradients—the effect is to integrate over planes that have some thickness. This is analogous to finite-width detectors in computed tomography.

Equation (43) is not in the form of the probe transform defined in (1). If, however, $\mathbf{p}(\boldsymbol{\omega}) \cdot \mathbf{v}(\mathbf{x})$ is small, then $\exp\{j\mathbf{p}(\boldsymbol{\omega}) \cdot \mathbf{v}(\mathbf{x})\} \approx 1 + j\mathbf{p}(\boldsymbol{\omega}) \cdot \mathbf{v}(\mathbf{x})$ and

$$z(l, \boldsymbol{\omega}) \approx \int \rho(\mathbf{x}) \delta(l - \mathbf{x} \cdot \boldsymbol{\omega}) d\mathbf{x} + j \int \rho(\mathbf{x}) \mathbf{v}(\mathbf{x}) \cdot \mathbf{p}(\boldsymbol{\omega}) \delta(l - \mathbf{x} \cdot \boldsymbol{\omega}) d\mathbf{x}. \quad (44)$$

Now consider the two measurements $z_0(l, \boldsymbol{\omega})$, acquired with $\mathbf{M}_1' = 0$, and $z_1(l, \boldsymbol{\omega})$, acquired with \mathbf{M}_1' not equal to zero but small enough so that the above approximation is valid. Then

$$\begin{aligned} g^P(l, \boldsymbol{\omega}) &= j[z_0(l, \boldsymbol{\omega}) - z_1(l, \boldsymbol{\omega})] \\ &= \int \mathbf{p}(\boldsymbol{\omega}) \cdot \rho(\mathbf{x}) \mathbf{v}(\mathbf{x}) \delta(l - \mathbf{x} \cdot \boldsymbol{\omega}) d\mathbf{x} \end{aligned} \quad (45)$$

is precisely a probe transform measurement of the vector field $\mathbf{q}(\mathbf{x}) = \rho(\mathbf{x}) \mathbf{v}(\mathbf{x})$. Additional probe directions can be acquired by changing \mathbf{M}_1' . In principle, three probe directions and (velocity-nulled) $z_0(l, \boldsymbol{\omega})$ are required to reconstruct $\mathbf{q}(\mathbf{x})$. The velocity itself can be reconstructed by dividing $\mathbf{q}(\mathbf{x})$ by $\rho(\mathbf{x})$, which is found by taking the inverse 3-D Radon transform of the measurements $z_0(l, \boldsymbol{\omega})$.

VI. SUMMARY AND CONCLUSION

This paper presented three new projection theorems for vector tomography. The third theorem was used to develop several new convolution backprojection reconstruction formulas for vector fields and their irrotational and solenoidal components. Significant simplification resulted when the probes were chosen as a 3-D right-handed orthonormal basis with $\boldsymbol{\omega}$ as one of the basis directions. These formulas and those of a previous paper were verified in simulation by synthetically scanning and reconstructing a vector field and its components. A limited data algorithm was also implemented and evaluated to demonstrate the local reconstruction property of these formulas. Finally, an approach to measure the 3-D probe transform using a magnetic resonance scanner was presented.

The theoretical results of this paper complete a basic analogy between vector tomography and standard computed tomography by developing projection theorems and convolution backprojection reconstruction formulas. Many other theoretical questions remain, including the issue of boundary conditions, which, as Braun and Hauck point out in [7], are often of critical importance in the study of vector fields. Also, the formulation and study of new transformations similar to the probe transform is of importance in some applications—e.g., magnetic resonance imaging—where approximations are required to cast the physical problem into the probe transform model. On the practical side, the implementation of the probe transform reconstruction formulas are scarcely more difficult than those for the standard inverse 3-D Radon transform. While the simulations presented herein used probes that comprise a 3-D right-handed orthonormal basis, it is important to realize that linear independence is all that is required, and that field components can be reconstructed from fewer than three probes. This may allow the use of the probe transform formalism in new applications. Finally, it should be noted that the approach used to generate simulations in this paper—i.e., synthetically scanning a discrete vector field and reconstructing the potentials or field components—represents (as far as we know) a completely new way to extract both potential functions and field components from a sampled vector field.

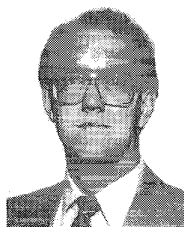
ACKNOWLEDGMENT

The author wishes to thank T. S. Denney, J. M. Weinfield, S. Gupta, W. Chiu, C. Davatzikos, E. Atalar, and N. Osman for their helpful discussions.

REFERENCES

- [1] S. A. Johnson, J. F. Greenleaf, M. Tanaka, and G. Flandro, "Reconstructing three-dimensional fluid velocity vector fields from acoustic transmission measurements," in *Acoustical Holography*, vol. 7, L. Kessler, Ed. New York: Plenum, 1977, pp. 307–326.
- [2] S. Takuso *et al.*, "Introduction of mass conservations law to improve the tomographic estimation of flow velocity distribution from differential time-of-flight data," *J. Acoust. Soc. Amer.*, vol. 77, no. 6, pp. 2104–2106, 1985.
- [3] G. Faris *et al.*, "Three-dimensional beam-deflection optical tomography of a supersonic jet," *Appl. Opt.*, vol. 27, no. 24, pp. 5202–5212, 1988.
- [4] W. Munk and C. Wunsch, "Ocean acoustic tomography: a scheme for large-scale monitoring," *Deep-Sea Research*, vol. 26A, pp. 123–161, 1979.

- [5] B. M. Howe, P. F. Worchester, and W. Munk, "Ocean acoustic tomography: Mesoscale velocity," *J. Geophys. Research*, vol. 92, pp. 3785–3805, 1987.
- [6] S. J. Norton, "Tomographic reconstruction of 2-D vector fields: application for flow imaging," *Geophys. J.*, vol. 97, pp. 161–168, 1988.
- [7] H. Braun and A. Hauck, "Tomographic reconstruction of vector fields," *IEEE Trans. Signal Processing*, vol. 39, no. 2, pp. 464–471, 1991.
- [8] D. Rouseff and K. B. Winters, "Two-dimensional vector flow inversion by diffraction tomography," *Inverse Problems*, vol. 10, pp. 687–697, 1994.
- [9] S. J. Norton, "Unique tomographic reconstruction of vector fields using boundary data," *IEEE Trans. Image Processing*, vol. 1, no. 3, pp. 406–412, July 1992.
- [10] P. Juhlin, "Principles of doppler tomography," Lund Inst. Technol., Dept. Math., Lund, Sweden, Tech. Rep. LUTFD2/(TFMA-92)/7002+17P, Aug. 1992.
- [11] J. L. Prince, "A 3-D projection theorem for vector tomography with application to MRI," in *Proc. 8th Workshop Image Multidimen. Signal Processing*, 1993, pp. 100–101.
- [12] M. Zahn, "Transform relationship between Kerr-effect optical phase shift and nonuniform electric field distributions," *IEEE Trans. Dielectr. Electr. Insulat.*, vol. 1, no. 2, pp. 235–246, 1994.
- [13] V. A. Sharafutdinov, *Integral Geometry of Tensor Fields*. VSP: 1994.
- [14] J. L. Prince, "Tomographic reconstruction of 3-D vector fields using inner product probes," *IEEE Trans. Image Processing*, vol. 3, no. 2, pp. 216–219, Mar. 1994.
- [15] L. Desbat and A. Wernsdorfer, "Direct algebraic reconstruction and optimal sampling in vector field tomography," *IEEE Trans. Signal Processing*, vol. 43, no. 8, pp. 1798–1808, Aug. 1995.
- [16] S. R. Deans, *The Radon Transform and Some of Its Applications*. New York: Wiley, 1983.
- [17] P. M. Morse and H. Feshbach, *Methods of Theoretical Physics*. New York: McGraw-Hill, 1953.
- [18] K. B. Winters and D. Rouseff, "A filtered backprojection method for the tomographic reconstruction of fluid vorticity," *Inverse Problems*, vol. 6, pp. L33–L38, 1990.
- [19] H. Barrett, "The Radon transform and its applications," in *Progress in Optics XXI*, E. Wolf, Ed. New York: Elsevier, 1984, pp. 217–286.
- [20] F. Natterer, *The Mathematics of Computerized Tomography*. New York: Wiley, 1986.
- [21] L. A. Shepp, "Computerized tomography and nuclear magnetic resonance," *J. Comput. Assist. Tomog.*, vol. 4, no. 1, pp. 94–107, 1980.
- [22] N. J. Pelc, R. J. Herfkens, A. Shimakawa, and D. R. Enzmann, "Phase contrast cine magnetic resonance imaging," *Magn. Resonance Quar.*, vol. 7, no. 4, pp. 229–254, 1991.
- [23] S. Ljunggren, "A simple graphical representation of Fourier-based imaging methods," *J. Magn. Resonance*, vol. 54, pp. 338–343, 1983.
- [24] P. R. Moran, "A flow velocity zeugmatographic interlace for NMR imaging in humans," *Magn. Resonance Imaging*, vol. 1, pp. 197–201, 1982.
- [25] P. Sprawls and M. J. Bronskill, Eds, in *Proc. Physics MRI '92 AAPM Summer Sch.*, Amer. Assoc. Physicists in Med., Amer. Inst. Physics, 1993.



Jerry L. Prince (S'78–M'83) received the B.S., M.S., and Ph.D. degrees in 1982, 1986, and 1988, respectively, from the Massachusetts Institute of Technology, all in electrical engineering and computer science.

He joined the technical staff at the Analytic Sciences Corporation (TASC) in Reading, MA, where he contributed to the design of an automated vision system for synthetic aperture radar imaging. He joined the faculty and the Johns Hopkins University in 1989, and has been an Associate Professor in the Department of Electrical and Computer Engineering since 1994. He holds joint appointments in the Department of Radiology and the Department of Biomedical Engineering. His current research interests are in image processing and computer vision with primary application to medical imaging. His major projects include magnetic resonance imaging of cardiac motion, 3-D brain image analysis, and vector tomography.

Dr. Prince is a member of the Sigma Xi professional society and Tau Beta Pi, Eta Kappa Nu, and Phi Kappa Phi honor societies. He is a former Associate Editor of *IEEE TRANSACTIONS ON IMAGE PROCESSING* and is a recipient of the 1993 National Science Foundation Presidential Faculty Fellows Award.